Published OnlineFirst August 4, 2010; DOI: 10.1158/0008-5472.CAN-10-0303

Gd-DTPA, enabling, jointly with the enhanced tumor accumulation provided by the EPR effect, the improved detection of solid tumors. We also showed that the micelles have continuous and strong anticancer effect, and enhance the MRI contrast of the tumor region in an orthotopic human pancreatic cancer xenograft model much more intensely than Gd-DTPA alone, although the diagnosis and treatment of pancreatic cancer has been considered to be the most difficult among digestive cancers. Thus, the Gd-DTPA/DACHPt–loaded micelles are expected not only to improve the effectiveness and safety of the incorporated drugs but also to assist in the real-time monitoring of the drug distribution and tumor accumulation, suggesting the great potential of visible DDSs.

Materials and Methods

Cancer cell lines and animals

Murine colon adenocarcinoma 26 (C-26) cells were kindly supplied by the National Cancer Center. The BxPC3 human pancreatic adenocarcinoma cell line was obtained from the American Type Culture Collection. C-26 and BxPC3 cells were maintained in RPMI 1640 (Sigma-Aldrich, Inc.) containing 10% fetal bovine serum in a humidified atmosphere containing 5% CO_2 at 37°C. CDF_1 mice and BALB/c nude mice (female; 18–20 g body weight; 6 weeks old) were purchased from Charles River Japan. All animal experiments were carried out in accordance with the policies of the Animal Ethics Committee of the University of Tokyo.

Preparation of Gd-DTPA/DACHPt–loaded micelles

PEG-*b*-P(Glu) [Mw_{PEG} = 12,000 Da; polymerization degree of P(Glu) = 20] block copolymer was synthesized according to the previously described method (28). Briefly, the *N*-carboxy anhydride of γ-benzyl L-glutamate (Sigma Chemical) was synthesized by the Fuchs-Farthing method using triphosgene. Then, *N*-carboxy anhydride of γ-benzyl L-glutamate was polymerized in DMF initiated by the primary amino group of CH_3O-PEG-NH_2 (Nippon Oil and Fats) to obtain PEG-*b*-poly (γ-benzyl-L-glutamate) (PEG-*b*-PBLG). The polymerization degree was verified by comparing the proton ratios of methylene units in PEG (-OCH_2CH_2-: δ = 3.7 ppm) and phenyl groups of PBLG (-$CH_2C_6H_5$: δ = 7.3 ppm) in ^{1}H nuclear magnetic resonance (NMR) measurement (solvent: DMSO-d_6; JEOL EX270, JEOL, Inc.). PEG-*b*-PBLG was deprotected by mixing with 0.5 N NaOH at room temperature to obtain PEG-*b*-P(Glu). Complete deprotection was confirmed by ^{1}H-NMR measurement (solvent: D2O; temperature: 25°C).

Gd-DTPA (Aldrich Chemical) was converted to sodium salt by adjusting the pH to 7 with NaOH, and it was lyophilized. A 5 mmol/L solution of bis(nitrato) (*trans-l*-1,2-diaminocyclohexane)platinum(II) [DACHPt(NO_3)$_2$; W.C. Heraeus GmbH & Co. KG] in water was mixed with the sodium salt of Gd-DTPA (5 mmol/L), and the solution was maintained for 24 hours at 37°C. Then, PEG-*b*-P(Glu) ([Glu] = 5 mmol/L) was added to this solution ([DACHPt]/[Glu] = 1.0) and reacted for 120 hours at 37°C to prepare Gd-DTPA/DACHPt–loaded micelles. The micelles were purified by dialysis against distilled water [molecular weight cutoff size (MWCO): 2,000; Spectra/Por-6, Spectrum Laboratories] and by ultrafiltration (MWCO: 30,000). The size distribution of the Gd-DTPA/DACHPt–loaded micelles was evaluated by a dynamic light scattering (DLS) measurement at 25°C using a Zetasizer Nano ZS90 (Malvern Instruments). The Pt and Gd contents of the micelles were determined by inductively coupled plasma–mass spectrometry (ICP-MS; 4500 ICP-MS, Hewlett Packard).

Fourier transform IR spectra of Gd-DTPA/DACHPt aqueous complex

Fourier transform IR (FT-IR) spectra were obtained using a FT-IR spectrophotometer (FT/IR 615, JASCO Corp.) with a resolution of 4 cm^{-1}. To characterize the interaction between Gd-DTPA and DACHPt, freeze-dried Gd-DTPA/DACHPt complex at 1:1, 1:5, and 1:10 mixing ratios was milled with KBr and then pressed into a disc for analysis.

Arsenazo III colorimetric assay

The absence of Gd^{3+} in the Gd-DTPA/DACHPt mixture was confirmed by using the arsenazo III method (29). Briefly, Gd-DTPA and DACHPt were mixed at 1:1 molar ratio (0.2 mmol/L) in water. Then, 0.5 mL of this solution was mixed with 0.5 mL of arsenazo III (0.2 mmol/L; Sigma-Aldrich). The absorbance spectra were measured with a spectrometer (V-570 UV/VIS/NIR Spectrophotometer, JASCO). A calibration curve was obtained by measuring the absorbance at 660 nm of a series of standard solutions of the arsenazo III/Gd^{3+} complex prepared by mixing solutions of $GdCl_3$ (Sigma-Aldrich) and arsenazo III in water. The pH of the solutions was maintained at 6.5.

Release rate of DACHPt and Gd-DTPA from the Gd-DTPA/DACHPt–loaded micelles

The release of DACHPt and Gd-DTPA complexes from the micelles was studied by the dialysis method. One milliliter of Gd-DTPA/DACHPt–loaded micelles solution was introduced in a dialysis bag (MWCO: 6,000) and incubated in 99 mL micelles in physiologic conditions (i.e., 10 mmol/L PBS plus 150 mmol/L NaCl at 37°C). The solution outside the dialysis bag was sampled at defined periods. The concentration of Pt and Gd was measured by ICP-MS. The UV-Vis spectra of Gd-DTPA, $GdCl_3$, and the solution outside the dialysis bag were recorded from 270 nm to 280 nm with a UV-Vis spectrometer (V-570 UV/VIS/NIR Spectrophotometer).

Kinetic stability of Gd-DTPA/DACHPt–loaded micelles

The stability of the Gd-DTPA/DACHPt–loaded micelles in physiologic conditions was determined by DLS and static light scattering using a Zetasizer Nano ZS90. The changes in the light scattering intensity were measured at defined time periods. In this analysis, a decrease in the light scattering intensity was associated with a decrease in the apparent molecular weight of the micelles and drug density inside the micelle core as well as in the micelle concentration. The size distribution of the Gd-DTPA/DACHPt–loaded micelles was simultaneously monitored.

Published OnlineFirst August 4, 2010; DOI: 10.1158/0008-5472.CAN-10-0303

Characterization of the r_1 relaxivities

The MR contrast effect of the magnetic nanoparticles was examined by measuring their proton longitudinal relaxivities, r_1, of which the definition is the slope of the concentration dependence given as $1/T_1 = 1/T_{10} + r_1[\mathrm{Gd}]$, where T_1 is the longitudinal relaxation time, $1/T_1$ is the longitudinal relaxation rate contrast in the presence of a paramagnetic species, and $1/T_{10}$ is the longitudinal relaxation rate contrast in the absence of a paramagnetic species. The T_1 of Gd-DTPA/DACHPt–loaded micelles, Gd-DTPA, or Gd-DTPA/DACHPt solution at 0.1, 0.2, 0.3, 0.4, and 0.5 mmol/L was measured at 37°C in water with a 0.59-T ^{1}H-NMR analyzer (JNM-MU25A, JEOL) with a standard inversion-recovery pulse sequence.

Cancer models

CDF_1 mice (female, 6 weeks old) were inoculated s.c. with C-26 cells (1×10^6/mL) and used for biodistribution study, antitumor activity assay, and MRI. BALB/c nude mice (female, 6 weeks old) were inoculated in the pancreas with BxPC3 cells for biodistribution study, antitumor activity assay, and MRI. For the latter model, the mice were anesthetized by isoflurane inhalation, and the pancreas was exposed and injected subserosally with 0.1 mL of BxPC3 cells (5×10^6/mL).

Biodistribution

Biodistribution studies were carried out on C-26 tumor–bearing mice at 10 days after implantation when the mean tumor volume was ~100 mm^3. Oxaliplatin, Gd-DTPA, or Gd-DTPA/DACHPt–loaded micelles were i.v. injected to mice at a dose of 100 μg per mouse on a Pt basis or 100 μg per mouse on a Gd basis. The mice were sacrificed after defined time periods (1, 4, 8, and 24 hours). Tumors, livers, kidneys, and spleens were excised. Blood was collected from the inferior vena cava, heparinized, and centrifuged to obtain the plasma. The samples were dissolved in HNO_3 and evaporated to dryness. The Pt and Gd concentrations were then measured by ICP-MS after the samples were redissolved in 5 N HCl.

In vivo MRI of Gd-DTPA/DACHPt–loaded micelles

MR images were obtained using a 4.7-T UNITY INOVA imaging spectrometer (Varian, Inc.) equipped with a birdcage-type RF coil, 66 mm in diameter. For the T1W of the mice, the following parameters were adopted: spin-echo method, repetition time (TR) = 500 ms, echo time (TE) = 15 ms, field of view (FOV) = 32 × 32 mm^2, matrix size = 256 × 256, and slice thickness = 2 mm. MR images were obtained from C-26 tumor– and BxPC3 tumor–bearing mice when the mean tumor volume was 100 and 400 mm^3, respectively. For all of the mice, transaxial T1W images were taken before injecting Gd-DTPA/DACHPt–loaded micelles as a control. The mice were anesthetized with 1.2% isoflurane during the MRI experiments. The mice were injected i.v. with 5 μmol/kg of Gd-DTPA alone or Gd-DTPA/DACHPt–loaded micelles. The transaxial T1W images were taken with a phantom containing water as a reference signal every 10 minutes for 4 hours. The images were analyzed using Mathematica (Wolfram Research, Inc.) and Excel (Microsoft, Inc.). For each time point, the same level of slices that included the center of the tumors was chosen and segmented by drawing a square that included the tumor area. The pixel intensities in the tissues were compared with the precontrast images and the phantom.

Assessment of therapeutic effect by MRI

MR images were obtained using a 7.0-T MRI scanner (magnet: Kobelco and Jastec; console: Bruker Biospin) with a birdcage-type RF coil, 35 mm in diameter (Rapid Biomedical). The experiment was carried out on BxPC3 tumor–bearing mice at 10 days after implantation when the average size of the tumor was ~60 mm^3. Mice (n = 2) were initially anesthetized with 3.0% isoflurane, orally intubated, and then ventilated with 2.0% isoflurane (Abbott Japan) and 1:2 O_2/room air gas mixture using a rodent ventilator (MRI-1, CWE, Inc.). During MRI scanning, rectal temperature was continuously monitored and maintained at 37.0 ± 0.5°C using a heating pad throughout all scans. T1W MRIs were obtained before and 2 hours after administration of the Gd-DTPA/DACHPt–loaded micelles. The Gd-DTPA/DACHPt–loaded micelles were injected i.v. at 8 mg/kg on a Pt base and 3 mg/kg on a Gd-DTPA base. The control mice were injected i.v. with 30 mg/kg of Gd-DTPA, and they were imaged before and 30 minutes after the injection. The drugs were injected on days 0, 4, 8, 11, and 18. T1W multislice two-dimensional spin echo MRI with fat suppression preparation was obtained with the following parameters: TR = 600 ms (respiratory gating of 100 rpm), TE = 9.5 ms, FOV = 32 × 32 mm^2, matrix size = 256 × 256, slice thickness = 1 mm, and average = 4. Slice orientation of the T1W was transaxial (18 slices, nongap) and horizontal (14 slice, nongap).

Image reconstruction and analysis were performed using ParaVision (version 4.0; Bruker Biospin) and ImageJ (version 1.43; NIH). Regions of interest were identified using a mouse atlas of anatomy, and the volume of the tumors was estimated by the following equation: $V = a \times b^2/2$, where a and b are the major and minor axes of the orthotopic tumors measured from the MR images.

Histology and immunohistochemistry

The excised samples were directly frozen in liquid N_2 for immunohistochemistry or fixed in 4% paraformaldehyde and then paraffin embedded to prepare them for H&E staining. Frozen samples were sectioned at 16-μm thickness in a cryostat, fixed in acetone, and incubated with protein blocking solution (Blocking One Buffer, Nakalai Tesque, Inc.), PECAM-1 (BD Pharmingen), Alexa Fluor 488 secondary antibody (Invitrogen Molecular Probes), and Hoechst (Sigma-Aldrich). The samples were observed by using a Zeiss LSM510 Meta confocal microscope for immunohistochemistry and an Olympus AX80 microscope for H&E staining.

Micro-synchrotron radiation X-ray fluorescence spectrometry analysis

Mice bearing BxPC3 orthotopic tumors were injected i.v. with doses of 3 mg/kg (on a Pt base) of Gd-DTPA/DACHPt–loaded micelles. Four hours after the injection, the mice were

Published OnlineFirst August 4, 2010; DOI: 10.1158/0008-5472.CAN-10-0303

sacrificed and the tumors were excised, frozen in liquid N_2, sliced at 16 μm using a cryostat, and fixed on a polypropylene sheet. Micro-synchrotron radiation X-ray fluorescence spectrometry (μ-SR-XRF) was performed using beamline 37XU (30) at SPring-8, operated at 8 GeV and ~100 mA. The tissue samples were irradiated with incident X-rays with an energy of 14 keV, a beam spot size of 1.3 × 1.3 μm^2, and an intensity of 10^{12} photons/s. The fluorescence X-rays were measured using a Si solid-state detector in air at room temperature. Each sample was mounted on an *x-y* translation stage. The fluorescence X-ray intensity was normalized by the incident X-ray intensity, I_0, to produce a two-dimensional elemental map.

Results

Characterization of Gd-DTPA/DACHPt–loaded micelles

The core-shell micellar nanocarriers with PEG palisade were prepared by preincubating Gd-DTPA and DACHPt at a 1:1 molar ratio for >10 hours in water and mixing this solution with PEG-*b*-P(Glu) (Fig. 1). The incubation of DACHPt with Gd-DTPA may lead to the formation of carboxylato complexes between DACHPt and the carboxylic groups in the DTPA chelator of Gd-DTPA. Accordingly, the FT-IR spectra of the DACHPt, Gd-DTPA, and Gd-DTPA/DACHPt mixtures incubated for 24 hours (Fig. 2A) indicated the appearance of a peak at 1,650 cm^{-1} in the spectra of the Gd-DTPA/DACHPt mixtures assigned to the Pt-COO coordination bond. Moreover, the optimal mixing ratio and incubation time of Gd-DTPA and DACHPt were determined by relaxivity titration. The r_1 of the Gd-DTPA/DACHPt complexes gradually increased up to 4.6 $mmol/L^{-1}s^{-1}$ at a 1:1 ratio from the initial 3.4 $mmol/L^{-1}s^{-1}$ of Gd-DTPA alone (Supplementary Fig. S1A). At DACHPt/Gd-DTPA ratios higher than 1, the r_1 remained constant. In addition, the r_1 of the Gd-DTPA/DACHPt complex gradually increased until 10 hours after mixing. Moreover, the activated state of DACHPt was found to be necessary for binding to Gd-DTPA because the Gd-DTPA/oxaliplatin mixture revealed no increase in the relaxivity (Supplementary Fig. S1B). During the Gd-DTPA/DACHPt complex formation, the stability of the Gd-DTPA complex was evaluated by using the arsenazo III method (29). Consequently, the absence of Gd^{3+}

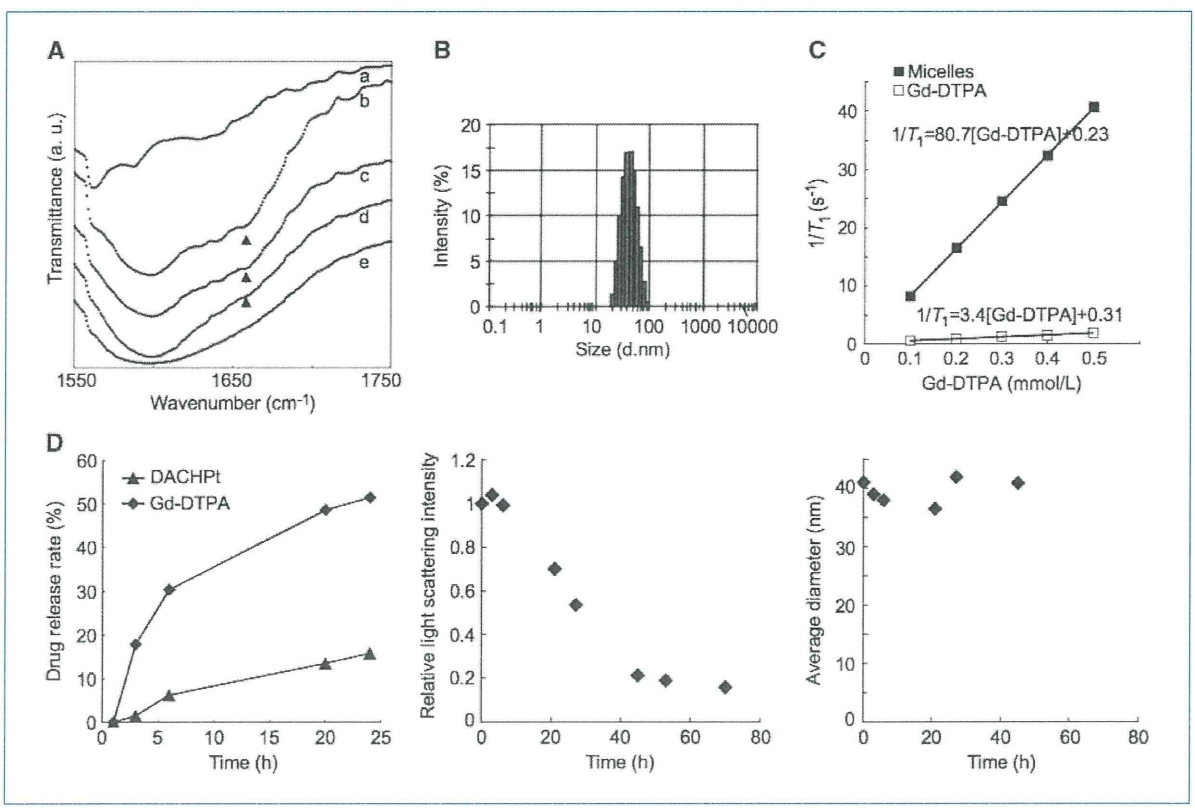

Figure 2. Formation and physicochemical characteristics of Gd-DTPA/DACHPt–loaded micelles. A, FT-IR spectra of DACHPt (a); Gd-DTPA/DACHPt complexes 1:1 (b), 5:1 (c), and 10:1 (d); and Gd-DTPA (e). B, diameter of the micelles determined by DLS. C, longitudinal relaxation ($1/T_1$) of micelles and Gd-DTPA at 37°C. The longitudinal relaxivities (r_1) were calculated from the slope. D, left, release rate of Pt and Gd complexes from Gd-DTPA/DACHPt–loaded micelles in physiologic conditions; middle, relative light scattering intensity of the Gd-DTPA/DACHPt–loaded micelles in physiologic conditions; right, diameter of Gd-DTPA/DACHPt–loaded micelles in physiologic conditions.

Published OnlineFirst August 4, 2010; DOI: 10.1158/0008-5472.CAN-10-0303

in the Gd-DTPA/DACHPt mixture was confirmed (Supplementary Fig. S2).

The obtained micelles were 33 nm in diameter with a narrow size distribution (polydispersity index = 0.067; Fig. 2B). This diameter might be small enough for the micelles to avoid recognition by the reticuloendothelial system, pass through the leaky vasculature of solid tumors by the EPR effect, and attain deep tumor penetration (17). The amounts of DACHPt and Gd-DTPA incorporated in the micelles were found to be 0.42 mg DACHPt/mg polymer and 0.04 mg Gd-DTPA/mg polymer, corresponding to 45% and 5% of the carboxylic groups in PEG-*b*-P(Glu), respectively. Moreover, the r_1 of the micelles increased up to 80.7 $mmol/L^{-1}s^{-1}$, that is, ~24-fold greater than Gd-DTPA alone (Fig. 2C).

The Gd-DTPA/DACHPt–loaded micelles did not release their contents in distilled water (data not shown). However, under physiologic conditions (i.e., 10 mmol/L PBS at 37°C), DACHPt and Gd-DTPA were released in a sustained manner (Fig. 2D, left). Moreover, the release of Gd-DTPA was considerably faster than that of DACHPt, probably due to stronger binding between polymer and DACHPt than between DACHPt and Gd-DTPA. In addition, the safe Gd-DTPA chelates in this system might remain stable because no free Gd^{3+} was detected in the released sample (Supplementary Fig. S3). The gradual drug release from Gd-DTPA/DACHPt–loaded micelles led to a reduction in the light scattering intensity of the micelles (Fig. 2D, middle) due to the decreased density of the micellar cores. Accordingly, the light scattering intensity of the Gd-DTPA/DACHPt–loaded micelles under physiologic conditions decreased to 20% in ~60 hours (Fig. 2D, middle); however, the hydrodynamic diameter of the micelles was maintained at ~30 nm for >48 hours (Fig. 2D, right). The high stability of the micelles and preservation of their hydrodynamic diameter are advantageous in the *in vivo* situation because the structural stability of micelles is highly associated with their prolonged blood circulation (11).

In vivo performance of Gd-DTPA/DACHPt–loaded micelles

The Gd-DTPA/DACHPt–loaded micelles extended the circulation of their cargo in the bloodstream, attaining ~20% of the injected dose of DACHPt after 24 hours and >8% of the injected dose of Gd-DTPA after 4 hours, whereas free oxaliplatin and free Gd-DTPA were rapidly cleared from plasma (Fig. 3A). Moreover, the micelles delivered the drugs to solid tumors due to the increased accumulation and retention at the cancer site because of the EPR effect. Accordingly, the micelles augmented the tumor accumulation 27.7 times for the Pt drug at 24 hours, and >100 times for Gd-DTPA at 4 hours, in subcutaneous murine colon adenocarcinoma 26 (C-26) tumors (Fig. 3B) compared with oxaliplatin and free Gd-DTPA, resulting in high MRI contrast enhancement of the tumor tissue (Fig. 3C). From the ratio of the signal intensities of tumor to muscle, the micelles showed to increase the contrast, whereas the enhancement for Gd-DTPA was almost unchanged. Moreover, the elevated tumor accumulation of Gd-DTPA/DACHPt–loaded micelles may also improve the antitumor activity of the incorporated Pt drug because DACHPt complexes can exert their cytotoxicity after being released from the Gd-DTPA/DACHPt–loaded micelles, as observed in *in vitro* studies (Supplementary Table S1). Accordingly, the micelles showed strong antitumor effect against the C-26 tumor model (Supplementary Fig. S4). Thus, we tested the potential of Gd-DTPA–loaded micelles for monitoring the drug distribution, tumor imaging, and treatment in a pancreatic tumor model close to the clinical situation (i.e., orthotopically inoculated BxPC3 human pancreatic ductal adenocarcinoma tumor).

Direct detection and treatment of pancreatic cancer

The T1W T_1-weighted MR images after i.v. administration of the Gd-DTPA/DACHPt–loaded micelles clearly showed specific contrast enhancement at the tumor area for >4 hours (Fig. 4A and B). In contrast, we did not observe any enhancement in the tumor region after the administration of free Gd-DTPA (Fig. 4A and B), and the signal intensity was higher in the liver, kidney, or spleen than in tumor as suggested from the tumor-to-organ ratios of the MR intensity (Supplementary Table S2). Also, the signals in all organs decreased after 1 hour. The macroscopic observation of the orthotopic tumor-bearing mice that received Gd-DTPA/DACHPt–loaded micelles confirmed the position of every organ and the tumor (Fig. 4D, left and middle), whereas the histologic study of the malignancy revealed the poorly differentiated histology of pancreatic adenocarcinoma, with thick fibrosis and low vascularization (Fig. 4D, right). The amount of Gd-DTPA delivered by the micelles in the orthotopic pancreatic tumor was seven times higher than the accumulation of free Gd-DTPA (Fig. 4C). Accordingly, 3.5% of the total Gd dose from the micelles and 7.2% of the total Pt dose had accumulated within 4 hours of administration.

The antitumor activity of Gd-DTPA/DACHPt–loaded micelles was also evaluated by MRI. Thus, the mice treated with the micelles at 8 mg/kg on a Pt base achieved a significant reduction in the volume of orthotopic BxPC3 tumors (Fig. 5A). Likewise, the weight of the pancreas at day 18 of the micelle-treated animal was much lower than the mice that received only Gd-DTPA (Fig. 5B). Moreover, Gd-DTPA/DACHPt–loaded micelles were shown to enhance the signal intensity at the tumor region (Fig. 5C). Thus, Gd-DTPA/DACHPt–loaded micelle can be used to follow the micelle accumulation in the tumor and the tumor size by MRI, supporting the theranostic concept.

The microdistribution of the drugs at the tumor site was studied using μ-SR-XRF on the pancreatic lesions. Besides the elements traditionally present in animal tissue, such as S, Cl, K, Ca, Fe, Cu, Ni, and Zn, very distinct Pt-L and Gd-L peaks can also be observed in the sum spectrum of the line scan. Thus, the distribution of several atoms (Fe, K, Gd, and Pt) in the tissue sections of the whole pancreas was studied to evaluate the tissue properties and layout of the drugs. The elemental mapping of Fe presents areas with high concentration probably involving the vicinity of blood vessels and the

Published OnlineFirst August 4, 2010; DOI: 10.1158/0008-5472.CAN-10-0303

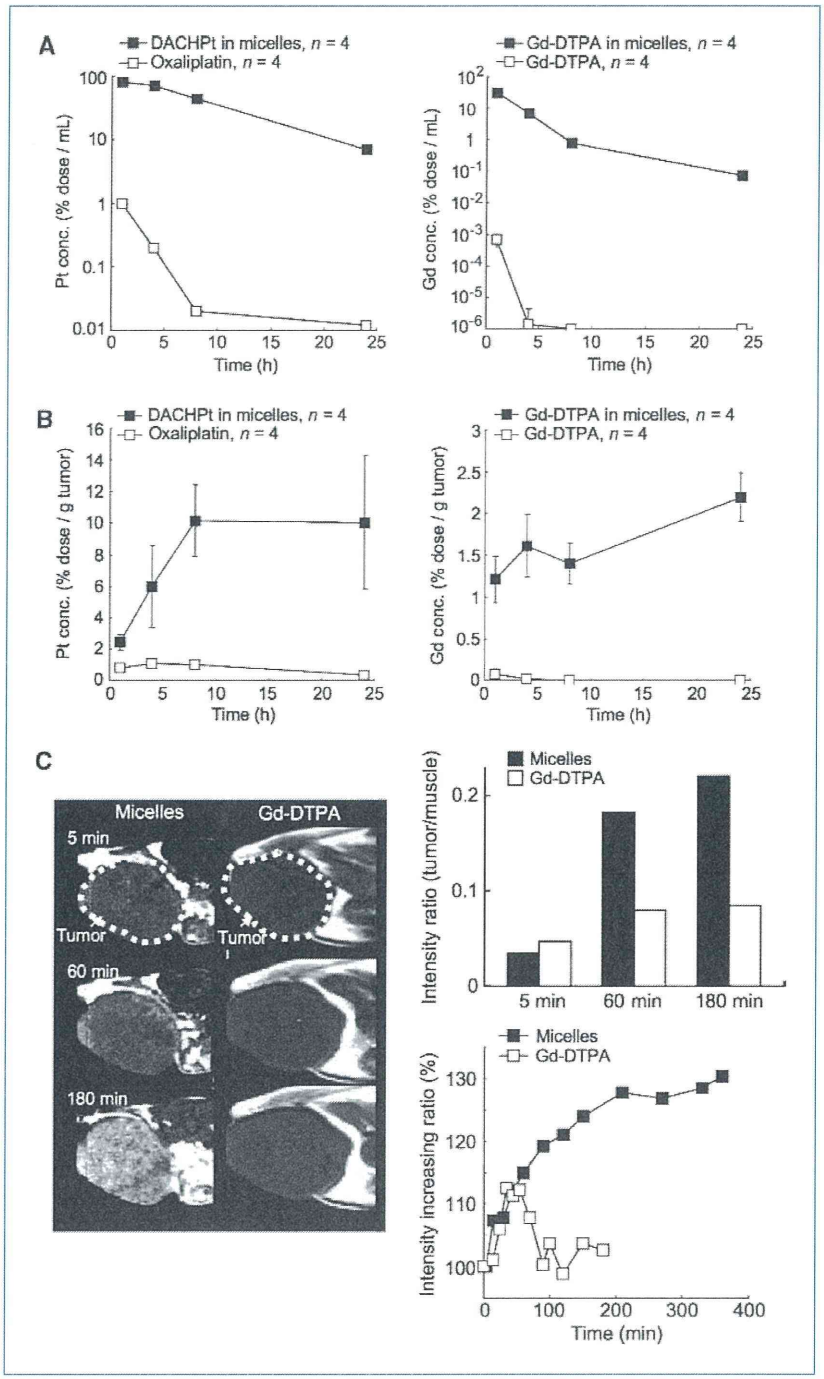

Figure 3. *In vivo* behavior of Gd-DTPA/DACHPt–loaded micelles. A, left, plasma clearance of Pt drugs after i.v. injection of oxaliplatin and Gd-DTPA/DACHPt–loaded micelles; right, plasma clearance of Gd complexes after i.v. injection of Gd-DTPA and Gd-DTPA/DACHPt–loaded micelles. B, left, accumulation of Pt drugs in the C-26 tumor after i.v. injection of oxaliplatin or Gd-DTPA/DACHPt–loaded micelles; right, accumulation of Gd complexes in C-26 tumors after i.v. injection of Gd-DTPA or Gd-DTPA/DACHPt–loaded micelles. C, left, *in vivo* MRI series of T_1-weighted transaxial slices of C-26 subcutaneous tumor after i.v. injection of Gd-DTPA/DACHPt–loaded micelles or Gd-DTPA at 5 μmol/kg Gd-DTPA. Right, top, tumor-to-muscle intensity ratio for the micelles and Gd-DTPA at 5, 60, and 180 min; bottom, relative intensity enhancement in the tumor after i.v. injection of Gd-DTPA/DACHPt–loaded micelles or Gd-DTPA at 5 μmol/kg Gd-DTPA.

distribution of heme proteins. Accordingly, the PECAM-1–positive area from the immunofluorescence microscopy (Fig. 6A) showing the existence of endothelial cells is consistent with this Fe-rich area (Fig. 6B). The K-rich regions possibly correspond to pancreatic cancer cells because K is a cofactor required to obtain maximum activity of the pyruvate kinase, an enzyme involved in glycolytic energy production, which has been observed in carcinoma tissue of the pancreas (31). The Gd as well as the Pt atoms located at those K-rich areas suggest the selective tumor accumulation of Gd-DTPA and DACHPt. Moreover, the colocalization of the Gd-DTPA and DACHPt confirms the high potential of Gd-DTPA/

Published OnlineFirst August 4, 2010; DOI: 10.1158/0008-5472.CAN-10-0303

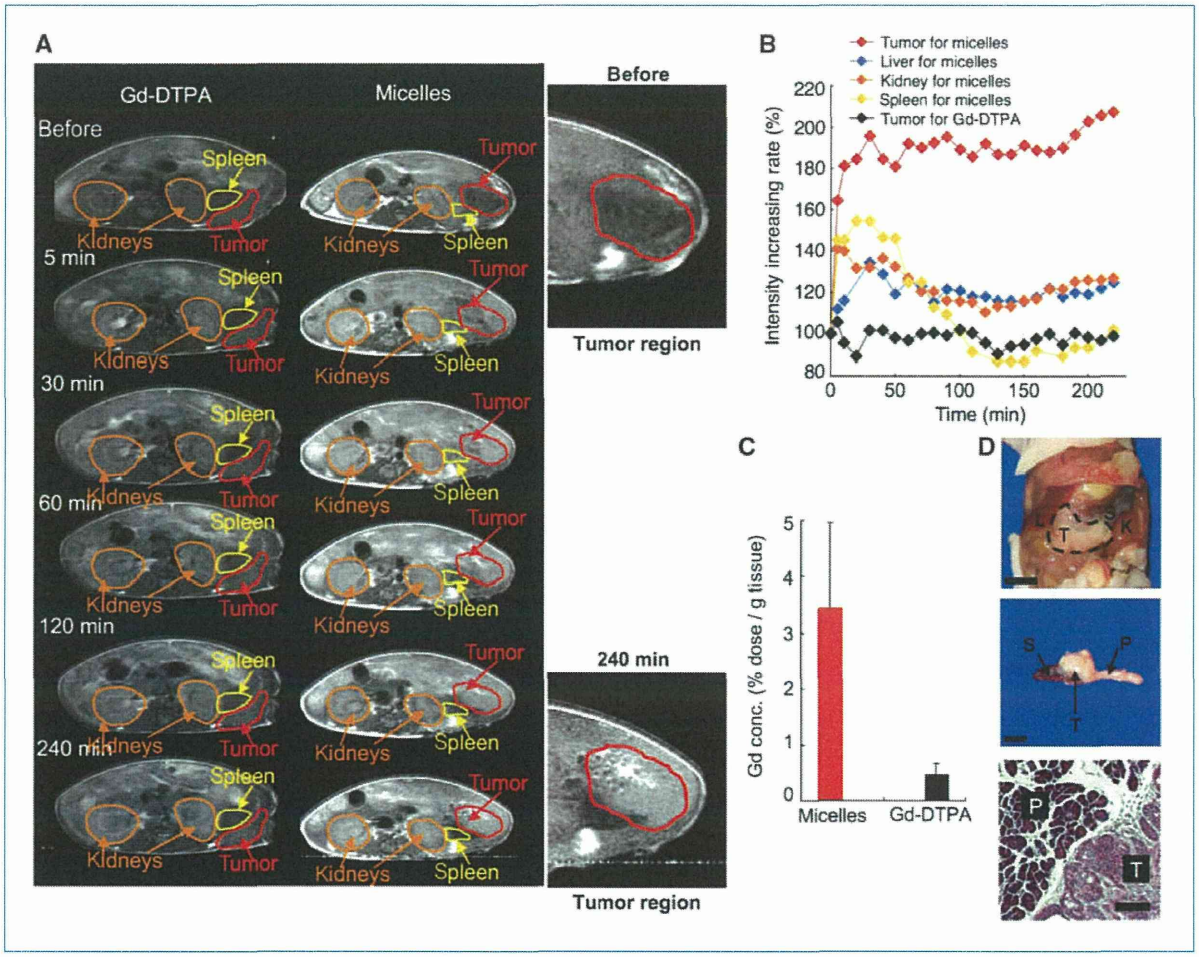

Figure 4. *In vivo* behavior of Gd-DTPA/DACHPt–loaded micelles on an orthotopic pancreatic cancer (BxPC3). A, *in vivo* MRI series of T_1-weighted transaxial slices of mice after i.v. injection of Gd-DTPA/DACHPt–loaded micelles or Gd-DTPA at 5 μmol/kg. B, relative MRI intensity in each organ after i.v. injection of Gd-DTPA/DACHPt–loaded micelles at 5 μmol/kg Gd-DTPA or i.v. injection of Gd-DTPA at 5 μmol/kg. C, the Gd-DTPA/DACHPt–loaded micelles and Gd-DTPA accumulation in the BxPC3 tumor 4 h after i.v. administration (n = 4). D, top, macroscopic findings of orthotopic BxPC3-bearing BALB/c nude mice after MRI acquisition. Scale bar, 1 cm. Pancreatic cancer (T), liver (L), kidney (K), and spleen (S). Middle, the pancreatic tumor after excision with spleen and normal pancreas. Scale bar, 0.5 cm. Bottom, microscopic findings (H&E staining) of the pancreatic cancer (T) and normal pancreatic tissue (P). Scale bar, 100 μm.

DACHPt–loaded micelles to assess the distribution of the anticancer drug at the tumor site by MRI.

Discussion

Pancreatic cancer has one of the worst prognoses among cancers (32). The high malignancy of pancreatic adenocarcinoma prompts the destruction of the surrounding tissue, whereas the lack of serous membrane in healthy pancreas cannot prevent the dissemination of cancer cells. The microenvironment characteristics of the pancreatic adenocarcinoma, including hypovascularity and thick fibrosis, prevent the accumulation of drugs in the tumor tissue (33). Moreover, the anatomic position of the pancreas in the deep retroperitoneal space makes early detection difficult. Although computed tomography is widely used for the evaluation of pancreatic carcinoma in the clinical setting, MRI may better predict the therapeutic efficacy and the prognosis in patients with pancreatic cancer because of its superior contrast resolution of noncontour deforming lesions of the pancreas, small liver metastases, and peritoneal disseminations (34). Thus, the outstanding contrast enhancement achieved by Gd-DTPA/DACHPt–loaded micelles on this tumor model suggests the great potential of this modality for the clear detection of the lesions in the abdominal cavity and the facile recognition of the carcinomas of the pancreas as distinct from the surrounding internal organs by MRI.

The exceptionally bright contrast achieved by Gd-DTPA/DACHPt–loaded micelles can be attributed to the enhanced accumulation of the micelles at the tumor site and to the

Published OnlineFirst August 4, 2010; DOI: 10.1158/0008-5472.CAN-10-0303

augmentation of the relaxivity of the Gd-DTPA in the core of the micelles. The amount of Gd-DTPA delivered by the micelles in the orthotopic pancreatic tumor was >3% of the injected dose after 4 hours. Because the r_1 of Gd-DTPA in the micelles is 24 times higher than that of free Gd-DTPA, the resulting contrast enhancement probably mimics a much higher accumulation level. In this regard, it has been reported that the r_1 of Gd-based MRI contrast agents increases after binding with polymers or proteins due to the flexibility reduction per Gd molecule and the increase of the rotational correlation time (τ_R; ref. 35). Moreover, Livramento and colleagues (36) suggested that an Fe/Gd chelate, a metallostar $Fe\{Gd_2(bipyridine(diethylenetriaminetetraacetic\ acid)_2(H_2O)_4)_3\}^{4-}$ structure, showed a high relaxivity because the inner-sphere water molecules presented an exchange rate (τ_m) close to the optimal value in addition to the increasing τ_R. In our system, the formation of the Gd-DTPA/DACHPt–loaded micelles probably combined an increase of the τ_R and the optimization of the τ_m in the hydrophobic environment at the micelle core, leading to the increase in relaxivity. Further studies are needed to establish the mechanism of the relaxivity enhancement of Gd-DTPA/DACHPt–loaded micelles, and they are currently under way in our laboratory.

The construction of macromolecular MRI contrast agents has been an attractive strategy to achieve diagnostic agents with extended blood circulation. Nevertheless, for Gd-based contrast agents, this approach could increase the risk of toxicity due to the prolonged tissue exposure to those macromolecules and the potential release of Gd^{3+} ions. Thus, the accumulation of high-generation dendrimer contrast agents in the healthy tissues might potentiate the nephrotoxicity and hepatotoxicity risks (37). Accordingly, only 20% of the injected dose of a generation 4–based PAMAM-Gd contrast agent was excreted from the body during the first 2 days, showing transient accumulation in the renal tubules. In contrast to this, the biodistribution of

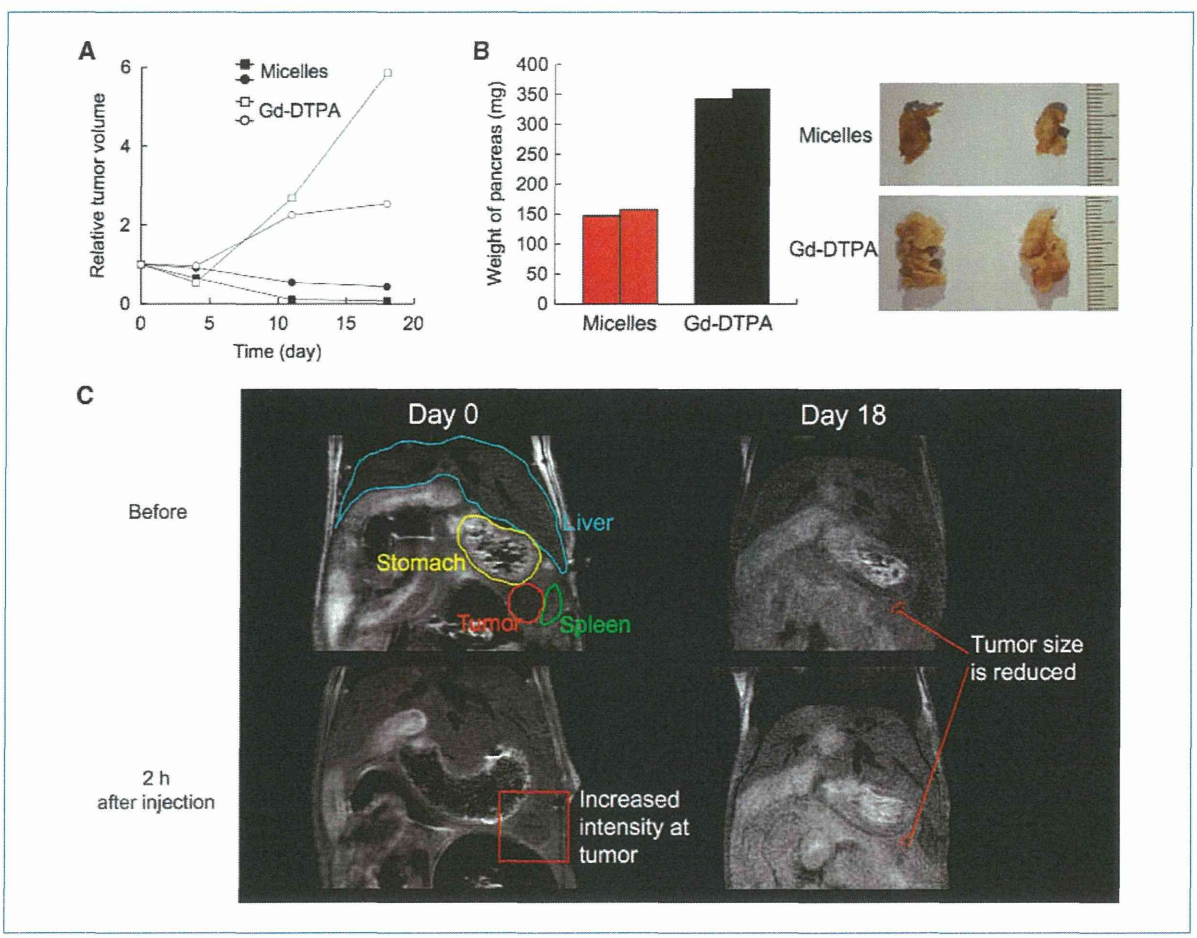

Figure 5. *In vivo* antitumor activity of Gd-DTPA/DACHPt–loaded micelles on orthotopic pancreatic cancer model (BxPC3) assessed by volumetric MRI. A, effect of Gd-DTPA/DACHPt–loaded micelles (8 mg/kg on Pt basis) and Gd-DTPA (30 mg/kg) injected i.v. at day 0, 4, 11 and 18 on the growth of BxPC3 tumors. B, left, weight of the whole pancreas for mice treated with the micelles or Gd-DTPA at day 18 on the antitumor experiment; right, macroscopies of the excised pancreas after treatment with the micelles or Gd-DTPA. C, MRI at days 0 and 18 of a tumor-bearing mouse treated with Gd-DTPA/DACHPt–loaded micelles. The tumor size was 89 mm^3 at day 0 and 5 mm^3 at day 18.

Published OnlineFirst August 4, 2010; DOI: 10.1158/0008-5472.CAN-10-0303

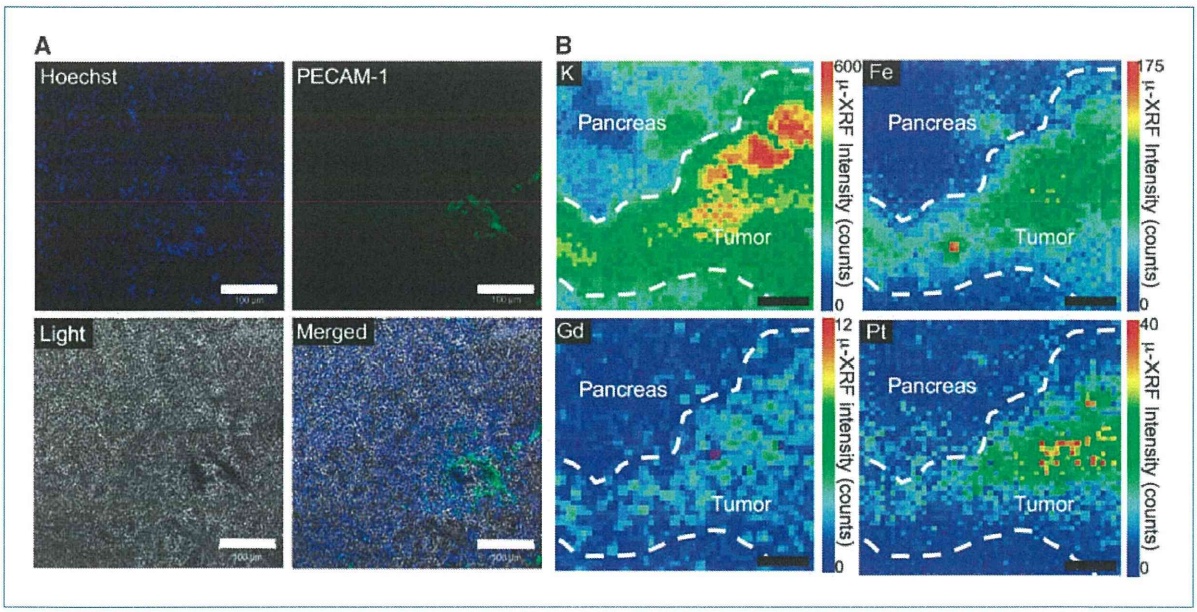

Figure 6. Intratumoral distribution of Gd-DTPA/DACHPt–loaded micelles in orthotopic BxPC3 tumors. A, immunofluorescence microscopy of tumor sections 4 h after injection of the micelles. The cell nuclei were stained with Hoechst, and the blood vessels were marked with PECAM-1 antibody. Scale bars, 100 μm. B, K, Fe, Pt, and Gd distribution in a tumor section including normal pancreatic tissue determined by μ-SR-XRF. Scale bars, 100 μm.

Gd-DTPA/DACHPt–loaded micelles revealed minimal accumulation of Gd-DTPA in normal tissues. Moreover, the Gd-DTPA released from the micelles probably is rapidly excreted from the body because of the relatively fast plasma clearance of low–molecular weight Gd-DTPA, thus eliminating the risk of undesired toxicity.

The real-time observation of drug distribution can increase the accuracy of treatment and enable practitioners to obtain feedback on the therapeutic efficacy at an earlier stage, and promptly adjust the treatment strategy. Gd-DTPA/DACHPt–loaded micelles might be helpful for directly assessing the distribution of the anticancer drugs at early stages by MRI. In this study, the μ-XRF results showed that the delivered Gd-DTPA and DACHPt were colocalized and uniformly distributed within the pancreatic tumors, whereas there was no drug accumulation in healthy pancreas, supporting the strong diagnostic and anticancer effect of the micelles (Fig. 6B, Pt and Gd). Moreover, the chemotherapy regimens are given in periodic cycles, for example, one cycle every 2 weeks during 12 weeks in FOLFOX (folinic acid, fluorouracil, and oxaliplatin) regimen for the treatment of colorectal cancer. By using Gd-DTPA/DACHPt–loaded micelles, the tumor size can be followed up in real-time by imaging at the day of the drug administration. Consequently, the Gd-DTPA/DACHPt–loaded micelles will have significant implications in the design and development of advanced multifunctional nanomedicines with great potential for clinical application as visible DDS.

Disclosure of Potential Conflicts of Interest

No potential conflicts of interest were disclosed.

Acknowledgments

We thank Sayaka Shibata and Teppei Nakahara for their technical assistance on the MRI experiments.

Grant Support

This research was supported by Funding Program for World-Leading Innovative R&D on Science and Technology (FIRST Program) from the Japan Society for the Promotion of Science (JSPS) and Grants-in-Aid for Scientific Research from the Japanese Ministry of Health, Labor, and Welfare (Nanomedicine Project).

The costs of publication of this article were defrayed in part by the payment of page charges. This article must therefore be hereby marked *advertisement* in accordance with 18 U.S.C. Section 1734 solely to indicate this fact.

Received 01/26/2010; revised 06/30/2010; accepted 07/09/2010; published OnlineFirst 08/04/2010.

References

1. Inoue A, Saijo Y, Maemondo M, et al. Severe acute interstitial pneumonia and gefitinib. Lancet 2003;361:137–9.
2. Jones BL. Trastuzumab: hopes and realities. Lancet Oncol 2002;3:137–44.
3. Ewer MS, Vooletich MT, Durand JB, et al. Reversibility of trastuzumab-related cardiotoxicity: new insights based on clinical course and response to medical treatment. J Clin Oncol 2005;23:7820–6.
4. Scappaticci FA, Skillings JR, Holden SN, et al. Arterial thromboembolic events in patients with metastatic carcinoma treated with chemotherapy and bevacizumab. J Natl Cancer Inst 2007;99:1232–9.

Published OnlineFirst August 4, 2010; DOI: 10.1158/0008-5472.CAN-10-0303

5. Davis ME, Chen Z, Shin DM. Nanoparticle therapeutics: an emerging treatment modality for cancer. Nat Rev Drug Discov 2008;7:771–82.
6. Torchilin VP. Recent advances with liposomes as pharmaceutical carriers. Nat Rev Drug Discov 2005;4:145–60.
7. Peer D, Karp JM, Hong S, Farokhzad OC, Margalit R, Langer R. Nanocarriers as an emerging platform for cancer therapy. Nature Nanotech 2007;2:751–60.
8. Ferrari M. Cancer nanotechnology: opportunities and challenges. Nat Rev Cancer 2005;5:161–71.
9. Duncan R. Polymer conjugates as anticancer nanomedicines. Nat Rev Cancer 2006;6:688–701.
10. Kabanov AV, Alakhov VY. Pluronic block copolymers in drug delivery: from micellar nanocontainers to biological response modifiers. Crit Rev Ther Drug Carrier Syst 2002;19:1–73.
11. Nishiyama N, Kataoka K. Current state, achievements, and future prospects of polymeric micelles as nanocarriers for drug and gene delivery. Pharmacol Ther 2006;112:630–48.
12. Matsumura Y, Kataoka K. Preclinical and clinical studies of anticancer agent-incorporating polymer micelles. Cancer Sci 2009;100:572–9.
13. Hashizume H, Baluk P, Morikawa S, et al. Opening between defective endothelial cells explain tumor vessel leakiness. Am J Pathol 2000;156:1363–80.
14. Maeda H. The enhanced permeability and retention (EPR) effect in tumor vasculature: the key role of tumor-selective macromolecular drug targeting. Adv Enzyme Regul 2001;41:189–207.
15. Muggia FM, Hainsworth JD, Jeffers S, et al. Phase II study of liposomal doxorubicin in refractory ovarian cancer: antitumor activity and toxicity modification by liposomal encapsulation. J Clin Oncol 1997;15:987–93.
16. Gradishar WJ, Tjulandin S, Davidson N, et al. Phase III trial of nanoparticle albumin-bound paclitaxel compared with polyethylated castor oil-based paclitaxel in women with breast cancer. J Clin Oncol 2005;23:7794–803.
17. Matsumura Y, Maeda H. A new concept for macromolecular therapeutics in cancer chemotherapy: mechanism of tumoritropic accumulation of proteins and the antitumor agent SMANCS. Cancer Res 1986;46:6387–92.
18. Hamaguchi T, Matsumura Y, Shirao K, et al. Phase I study of novel drug delivery system, NK911, a polymer micelle encapsulated doxorubicin [abstract 571]. Proceedings of the 39th annual meeting of the American Society of Clinical Oncology (ASCO); 2003, May 31-June 3; Chicago, USA.
19. Kato K, Hamaguchi T, Yasui H, et al. Phase I study of NK105, a paclitaxel-incorporating micellar nanoparticle, in patients with advanced cancer. ASCO Annual Meeting Proceedings. J Clin Oncol 2006;24:2018.
20. Burris HA III, Infante JR, Spigel DR, et al. A phase I dose-escalation study of NK012. ASCO Annual Meeting Proceedings. J Clin Oncol 2008;26:2538.
21. Wilson RH, Plummer R, Adam J, et al. Phase I and pharmacokinetic study of NC-6004, a new platinum entity of cisplatin-conjugated polymer forming micelles. J Clin Oncol 2008;26:2573.
22. Dent R, Trudeau M, Pritchard KI, et al. Triple-negative breast cancer: clinical features and patterns of recurrence. Clin Cancer Res 2007;13:4429–34.
23. McCarthy JR, Weissleder R. Multifunctional magnetic nanoparticles for targeted imaging and therapy. Adv Drug Deliv Rev 2008;60:1241–51.
24. McCarthy JR, Jaffer FA, Weissleder R. A macrophage-targeted theranostic nanoparticle for biomedical applications. Small 2006;2:983–7.
25. Pan D, Caruthers SD, Hu G, et al. Ligand-directed nanobialys as theranostic agent for drug delivery and manganese-based magnetic resonance imaging of vascular targets. J Am Chem Soc 2008;130:9186–7.
26. Nasongkla N, Bey E, Ren J, et al. Multifunctional polymeric micelles as cancer-targeted, MRI-ultrasensitive drug delivery systems. Nano Lett 2006;6:2427–30.
27. Weinmann HJ, Brasch RC, Press WR, Wesbey GE. Characteristics of gadolinium-DTPA complex: a potential NMR contrast agent. Am J Roentgenol 1984;142:619–24.
28. Cabral H, Nishiyama N, Okazaki S, Koyama H, Kataoka K. Preparation and biological properties of dichrolo(1,2-diaminocyclohexane) platinum(II) (DACHPt)-loaded polymeric micelles. J Control Release 2005;101:223–32.
29. Gouin S, Winnik F. Quantitative assays of the amount of diethylenetriaminepentaacetic acid conjugated to water-soluble polymers using isothermal titration calorimetry and colorimetry. Bioconjug Chem 2001;12:372–7.
30. Terada Y, Goto S, Takimoto N, et al. Construction and commissioning of BL37XU at SPring-8. AIP Conf Proc 2004;705:376–9.
31. Ventrucci M, Cipolla A, Racchini C, Casadei R, Simoni P, Gullo L. Tumor M2-pyruvate kinase, a new metabolic marker for pancreatic cancer. Dig Dis Sci 2004;49:1149–55.
32. Jemal A, et al. Cancer statistics, 2007. CA Cancer J Clin 2007;57:43–66.
33. Sofuni A, et al. Differential diagnosis of pancreatic tumors using ultrasound contrast imaging. J Gastroenterol 2005;40:518–25.
34. Miller FH, Rini NJ, Keppke AL. MRI of adenocarcinoma of the pancreas. Am J Roentgenol 2006;187:W365–374.
35. Zhang Z, Greenfield MT, Spiller M, McMurry TJ, Lauffer RB, Caravan P. Multilocus binding increases the relaxivity of protein-bound MRI contrast agents. Angew Chem 2005;117:6924–7.
36. Livramento JB, Toth E, Sour A, Borel A, Merbach AE, Ruloff R. High relaxivity confined to a small molecular space: a metallostar-based potential MRI contrast agent. Angew Chem Int Ed 2005;44:1480–4.
37. Duncan R, Izzo L. Dendrimer biocompatibility toxicity. Adv Drug Deliv Rev 2005;57:2215–37.

Cancer Science
The official journal of the Japanese Cancer Association

Hypoglycemic/hypoxic condition *in vitro* mimicking the tumor microenvironment markedly reduced the efficacy of anticancer drugs

Hiroko Onozuka,[1,2] Katsuya Tsuchihara[1] and Hiroyasu Esumi[1,2,3]

[1]Cancer Physiology Project, Research Center for Innovative Oncology, National Cancer Center Hospital East, Kashiwa, Chiba; [2]Department of Integrated Biosciences, Graduate School of Frontier Sciences, The University of Tokyo, Kashiwa, Chiba, Japan

(Received November 23, 2010/Revised January 14, 2011/Accepted January 18, 2011/Accepted manuscript online January 21, 2011/Article first published online March 7, 2011)

Tumor tissues are often hypoxic because of defective vasculature. We previously showed that tumor tissues are also often deprived of glucose. The efficacy of anticancer drugs is affected by the tumor microenvironment, partly because of the drug delivery and cellular drug resistance; however, the precise mechanisms remain to be clarified. In the present study, we attempted to clarify whether hypoglycemic/hypoxic condition, which mimics the tumor microenvironment, might induce drug resistance, and if it did, to elucidate the underlying mechanisms. Pancreatic cancer-derived PANC-1 cells were treated with serial dilutions of anticancer drugs and incubated in either normoglycemic (1.0 g/L glucose) or hypoglycemic (0 g/L glucose) and normoxic (21% O_2) or hypoxic (1% O_2) conditions. The 50% inhibitory concentration of gemcitabine was 1000 times higher for PANC-1 cells incubated under the hypoglycemic/hypoxic condition than for those incubated under the normoglycemic/normoxic condition. Conventional anticancer drugs target rapidly growing cells, so that non-proliferating or slowly proliferating cells usually show resistance to drugs. Though the cell cycle was delayed, sufficient cellular uptake and DNA incorporation of gemcitabine occurred under the hypoglycemic/hypoxic condition to cause DNA lesions and S-phase arrest. To overcome hypoglycemic/hypoxia-induced drug resistance, we examined kinase inhibitors targeting Chk1 or cell-survival signaling pathways. Among the compounds examined, the combination of UCN-01 and LY294002 partially sensitized the cells to gemcitabine under the hypoglycemic/hypoxic condition. These findings suggested that the adoption of suitable strategies may enhance the cytotoxicities of clinically used anticancer drugs against cancer cells. (*Cancer Sci* 2011; 102: 975–982)

It is widely accepted that solid tumors are heterogeneous in structure as a result of unregulated cancer cell proliferation, presence of several cell types and aberrant vessel formation. Among these, the tumor vasculature has a major impact on the tumor microenvironment. In normal tissue, vascular networks generally develop in a well-ordered hierarchal fashion, so that an insufficient blood supply seldom occurs. In contrast, tumor vascular networks undergo continuous remodeling, because unregulated cell proliferation destroys the existing tissue structures. Previous structural analyses had clearly shown that tumors exhibit aberrant and poorly organized vasculature without any hierarchy.[1–4]

As a consequence of the poorly organized vasculature in tumors, the delivery of oxygen is extremely limited. Direct measurement of the oxygen tension in cancer tissues has demonstrated the presence of severely hypoxic regions in many types of cancers.[5] Although hypoxia is also toxic to cancer cells, cancer cells adapt through genetic and epigenetic changes that allow them to survive and even proliferate in hypoxic environments.[6–9] Hypoxia-inducible factor-1α (HIF-1α) is a key transcription factor for downstream hypoxia-inducible genes, which regulate several biological processes in hypoxic environments.[10–12] Hypoxia response pathways overlap with many of the known oncogenic signaling pathways and also contribute to tumor aggressiveness.[13–15] Therefore, tumor hypoxia is regarded as a good target for cancer therapy. Meanwhile, cancer cells predominantly use the glycolytic pathway, rather than oxidative phosphorylation, for energy production, irrespective of the oxygen availability (Warburg effect).[16,17] In addition to the intrinsic predisposition of cancer cells to metabolize glucose, HIF-1α has been shown to regulate the expressions of all the enzymes involved in the glycolytic pathway, which mediate cellular glucose uptake.[18,19] The activation of HIF-1α enables cancer cells to use excessive glucose to maintain cellular homeostasis in hypoxic environments, causing depletion of glucose from the surrounding tissues. Indeed, a metabolomic analysis of stomach and colon cancer tissues has clearly showed glucose depletion in the tumor tissues as compared to normal tissues, indicating that several regions of tumor tissues are characterized by both hypoxia and hypoglycemia.[20] However, little is known about the biology of cancer cells under hypoglycemic condition.

Although many molecular-targeting drugs have been introduced for clinical use, conventional anticancer drugs are in wide clinical use and continue to confer many clinical benefits. Heterogeneity in the tumor microenvironment provides cancer cells the opportunity to escape from anticancer drugs. One of the processes affected by the heterogeneity of tumors is drug diffusion.[21,22] In addition, many types of drug resistance of the cells to anticancer drugs are known to occur, and overexpression of the ABC transporter is a representative mechanism.[23–25] Recent studies have reported that drug resistance may also be related to the tumor microenvironment, especially hypoxia, and the clinical relevance of such resistance. Three-dimensional culture system is used as a useful new strategy to represent tumor microenvironment *in vitro*.[26,27] However, the detailed molecular mechanisms for the resistance are largely unclear. In this study, we clarified how hypoglycemic/hypoxic condition might affect the efficacies of anticancer drugs.

Materials and Methods

Cell lines and culture conditions. The human pancreatic ductal adenocarcinoma cell lines PANC-1 and Capan-1 and the hepatoma-derived cell line HepG2 were purchased from ATCC (American Type Culture Collection, Rockville, MD, USA). PSN-1 was gifted from the Genetics Division of the National Cancer Center Research Institute (Tokyo, Japan). All cell lines were maintained in DMEM (Nissui, Tokyo, Japan). A

[3]To whom correspondence should be addressed. E-mail: hesumi@east.ncc.go.jp

doi: 10.1111/j.1349-7006.2011.01880.x